The Astrophysical Journal, 852:14 (8pp), 2018 January 1 https://doi.org/10.3847/1538-4357/aa9c7f

Particles Co-orbital to Janus and to Epimetheus: A Firefly Planetary Ring

Othon C. Winter[1], Alexandre P. S. Souza[1], Rafael Sfair[1],
Silvia M. Giuliatti Winter[1], Daniela C. Mourão[1], and Dietmar W. Foryta[2]
[1] São Paulo State University—UNESP, Grupo de Dinâmica Orbital & Planetologia, Guaratinguetá, CEP 12516-410, SP, Brazil; ocwinter@gmail.com
[2] Universidade Federal do Paraná—UFPr, Curitiba, PR, Brazil
Received 2017 January 11; revised 2017 November 16; accepted 2017 November 20; published 2017 December 28

Abstract

The *Cassini* spacecraft found a new and unique ring that shares the trajectory of Janus and Epimetheus, co-orbital satellites of Saturn. Performing image analysis, we found this to be a continuous ring. Its width is between 30% and 50% larger than previously announced. We also verified that the ring behaves like a firefly. It can only be seen from time to time, when *Cassini*, the ring, and the Sun are arranged in a particular geometric configuration, in very high phase angles. Otherwise, it remains "in the dark," invisible to *Cassini*'s cameras. Through numerical simulations, we found a very short lifetime for the ring particles, less than a couple of decades. Consequently, the ring needs to be constantly replenished. Using a model of particle production due to micrometeorites impacts on the surfaces of Janus and Epimetheus, we reproduce the ring, explaining its existence and the "firefly" behavior.

Key words: planets and satellites: dynamical evolution and stability – planets and satellites: individual (Epimetheus, Janus) – planets and satellites: rings

1. Introduction

Among its early findings, the *Cassini* Imaging Team discovered a ring occupying the region of the trajectories of the satellites Janus and Epimetheus (Porco et al. 2006). These two Saturnian satellites are well known for being the only co-orbital system with comparable masses (Dermott & Murray 1981; Harrington & Seidelmann 1981; Synnott et al. 1981; Yoder et al. 1983; Treffenstädt et al. 2015). As a consequence, they share the same mean orbit in horseshoe trajectories. The discovery of a ring of particles also sharing the same orbital region makes the whole system even more complex.

In the current work, we investigate some basic features of this ring through analysis of *Cassini* images. Is it a full ring or just a set of arcs? How wide is the ring? What is its radial profile? Then we numerically explore the lifetime of these particles, taking into account both gravity from Janus and Epimetheus and solar radiation pressure. We find that the particles stay in the co-orbital region for just a few decades. As it is highly improbable that this is a temporary ring, we studied a physical model of particles production that could maintain the ring. The model is based on hypervelocity impacts of micrometeorites onto the surface of the co-orbital satellites.

The structure of this paper is as follows. The next section presents the photometric analysis of the images. Section 3 describes our examination of the particles' lifetime through a sample of numerical simulations. The collisional model of particle production for the Janus–Epimetheus ring are given in Section 4. In the last section, we summarize our conclusions.

2. Photometric Analysis

Our starting point to search for *Cassini* images that could have captured the Janus–Epimetheus ring was the press release image W1537029133 obtained in 2006 September 15 (2006-258). We have used the OPUS tool provided by the Ring-Moon system node of NASA's Planetary Data System to search images acquired in an interval of two days prior and two days after 2006-258 (ISS_028RI_HIPHASE001_VIMS). We limited the results to data from both Wide Angle Camera (WAC) and Narrow Angle Camera (NAC) obtained through the clear filters (CL1 and CL2), which have a transmission band in the interval of 400–1000 nm for WAC, and 200–1000 nm for NAC (Porco et al. 2004). Using these parameters, 172 images (50 from NAC and 122 from WAC) were retrieved.

A visual inspection was carried out to remove those images where the ring region would be out of the field of view (FOV) or those where the ring region is saturated. After this process, the initial set was reduced to only 16 WAC images, all from the same day of PIA 08322, which are potentially useful for our purposes (Table 1). The best image of the ring obtained by the *Cassini* wide angle camera is shown in Figure 1 (top panel).

At different geometries, with phase angles between zero and 150° images W1575913637, W1524966389, W1594709597, W1622272726, W1490835963, and W1615207585, the search for images was made using the OPUS tool for the same camera (WAC), the same filters (CL1 and CL2), and looking for regions that cover the location of the ring (nearby the orbits of Janus and Epimetheus).

2.1. Calibration

The selected images were calibrated using the standard CISSCAL v.3 pipeline (Porco et al. 2004), which provides an interactive tool to subtract instrumental backgrounds, to compensate the uneven bit weighting and optical distortions, as well as to correct the pixel-to-pixel relative sensitivity using the flatfield frames. We choose to convert the image count to normalized units of I/F, where I is the intensity received from the ring and πF is the solar flux at the distance of Saturn. The normalization is such that $I/F = 1$ for a perfectly reflecting Lambert surface illuminated and viewed from normal incidence.

In some cases, an additional step was applied to smooth the image, where we have used a moving box to replace the value of each pixel by the median of the surrounding pixels. This procedure removes cosmic rays and high-frequency noise in the image, making the ring easier to detect and quantify. It was used when was necessary to obtain the radial profile.

Table 1
Summary of the Useful Images Retrieved from PDS Ring Node

Image	Time (day 258)	Exposure Time (ms)	$\Delta\theta$ (°)	Phase Angle (°)
W1537006439	09:42:15.769	80	159	177.2–179.5
W1537006505	09:43:21.805	15	159	177.2–175.5
W1537007792	10:04:48.760	80	119	177.1–179.1
W1537007825	10:05:21.614	380	119	177.1–179.1
W1537008000	10:08:16.793	50	119	177.1–179.1
W1537009120	10:26:56.752	80	119	177.1–179.1
W1537011801	11:11:37.734	80	67	176.9–177.7
W1537011834	11:12:10.588	380	67	176.9–179.2
W1537028326	15:47:02.613	80	144	176.3–179.2
W1537028414	15:48:30.654	20	144	176.3–179.2
W1537028438	15:48:53.068	3200	144	176.3–179.2
W1537028473	15:49:29.080	1200	144	176.3–176.2
W1537028702	15:53:18.611	80	49	176.6–179.5
W1537029078	15:59:34.608	80	145	175.5–178.4
W1537029133	16:00:29.581	150	145	175.5–178.4
W1537029166	16:01:02.650	20	145	175.5–178.4
W1537029190	16:01:25.063	3200	145	175.5–178.4

Note. The time corresponds to the MID_TIME of each frame and $\Delta\theta$ is the azimuthal coverage of the ring. The image W1537029133 was identified as PIA 08322. In bold is indicated the best image found.

2.2. SPICE Navigation

The images were navigated using the SPICE routines and the appropriate kernels for the given time interval of the observations. First, we have computed the position of the spacecraft and the Sun relative to a body-fixed rectangular frame centered on Saturn (IAU_SATURN), for which the reference plane coincides with the plane of the rings (assumed to be the equatorial). We were also able to determine the instrument FOV, as well as the pointing vector and the ring plane intercept of each pixel.

From the pointing vector, we can determine the radial and longitudinal positions of every pixel in the ring plane, as well as the illumination angles, and the phase angle (α). In order to check the accuracy of our code, we selected some high-resolution images, for which we could successfully determine the radial position of the narrow Keeler gap.

Due to the geometry of the observation and the instrument characteristics, each image covers a wide range of co-rotating longitudes. To measure the azimuthal amplitude, we determine those pixels located at the radial distance of the ring and then calculate the longitudinal position of the extremes of the arc in the IAU_SATURN frame. When the longitudes are converted to a synodic system that rotates with the angular velocity of the satellites, we see that three images are enough to cover 320° (Figure 2), confirming the fact that the observed structure is indeed a complete ring. We do not detect any obvious longitudinal brightness variations in the ring.

2.3. Radial Profile

The ring is tenuous and it is in a region that also contains a broad dust population extending from the F to the G ring, and so it is not possible to safely distinguish the ring profile when taken across a single line of the image. As an alternative, from image W1537029133 (top panel of Figure 1), we extracted multiple radial scans and combined them to produce a better and smoother profile where the ring is clearly visible (bottom panel of Figure 1).

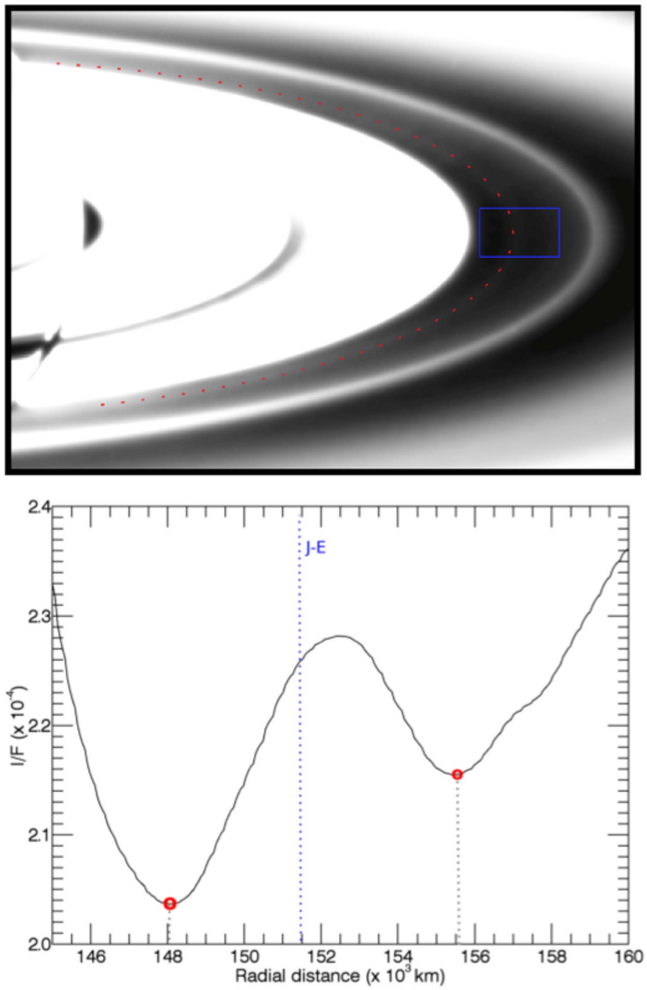

Figure 1. Saturn's rings image (W1537029133) from the *Cassini* spacecraft camera (top panel). The location of the Janus–Epimetheus ring is indicated by the red dashed line. A plot of the I/F for the region indicated by the small blue box is presented in the bottom panel. This plot also shows the width of the ring (≈7500 km) and the location of averaged orbits of the co-orbital moons, Janus and Epimetheus. Note an asymmetry: the peak does not coincide with the mean orbital radius of the co-orbital moons.

In the bottom panel of Figure 1, the I/F ratio is plotted as a function of the radial distance from Saturn. Based on two local minima, we measured the width of the ring as approximately 7500 ± 500 km, assuming an error up to one pixel. This is approximately 50% larger than previously announced (Porco et al. 2006).

The estimated peak value of I/F for the ring is $\sim 2.4 \times 10^{-5}$. This value is obtained by the difference between the ring peak and the background, which is assumed to be constant and equal to the value of the ring minimum at the inner edge (left red dot). It is worth pointing out that all of these quantities are consistent with two other images from where suitable radial profiles could be obtained by the same process of combination of multiple scans at different longitudes.

It can be seen that the ring presents an asymmetry, being brighter in the outward region. It is an unexpected feature, as the impact mechanism and the later evolution of the particles tend to spread the particles in such a manner as to produce a symmetrical profile whose peak is aligned with the source

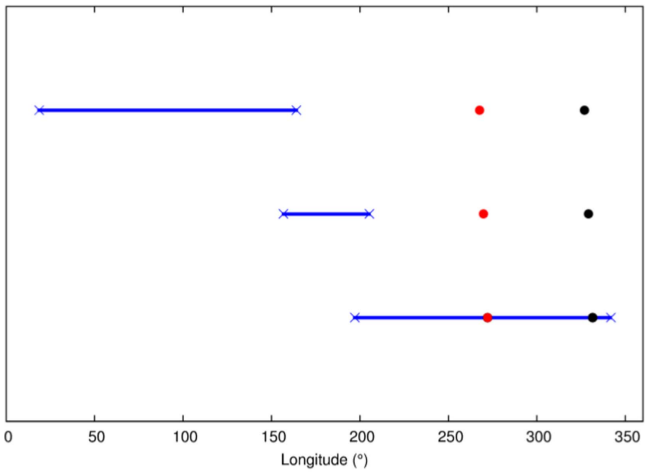

Figure 2. Longitudinal coverage of the ring for three different images measured in a frame that rotates with angular velocity equal to the mean motion of the satellites. For each image, the positions of Janus and Epimetheus are represented by red and black dots, respectively. Note that the zero point of this longitude is arbitrarily set for display purposes. From top to bottom, the data correspond to images W1537028326, W1537028702, and W1537029078.

bodies. In our analysis, the peak of brightness is located at 152,359 km, ~920 km outside the orbits of the satellites, and a possible explanation is that the outer region of the ring is more affected by light contamination due to the proximity with the G ring. In the case of the background being considered as a straight line between the two minima, which is an extreme assumption, the I/F value would be 1.9×10^{-5}, i.e., about 20% smaller. So, in this paper, we will be considering values of I/F that are at most 20% larger than the case assuming an extreme background model. Still, if we suppose that the maximum of brightness of the ring matches the orbit of Janus and Epimetheus (blue line), and they mirror the inner part of the ring to the right side, the ring maximum I/F decreases to 2.3×10^{-5} and its width is reduced by 700 km, which is still 36% larger than previously thought.

2.4. Photometry

By calibrating and analyzing each image of the set of images that could have captured the J–E ring, we found that the ring was visible in images with very high phase angles (Sun-ring-*Cassini*), $175\overset{\circ}{.}4 \leqslant \alpha \leqslant 179\overset{\circ}{.}8$, indicating the strong forward scattering nature of the ring. This behavior, along with the non-detection of the ring in observations of the same region made by *Cassini* at different geometries ($\alpha \sim 24°$, ~34°, ~65°, ~78°, ~97°, ~127°), indicate that the Mie theory should be a useful approximation for a particle size distribution dominated by micrometric grains (van de Hulst 1957). Following van de Hulst (1957) and Gumprecht & Sliepcevich (1953), we can place an upper limit of the sizes of observable particles as 20 times the incident wavelength, which corresponds to approximately 13 μm in radius. Therefore, despite being a continuous full ring, it still can only be seen by *Cassini*'s camera at very high phase angles.

For the images listed in Table 1, a visual inspection does not reveal any clump or gap along the ring azimuth, and the ring appears to be azimuthally uniform. The variation of the ring brightness depends only on the change of the phase angle. In addition, the ring's absolute brightness depends on the emission angle of the pointing vector of each pixel, because incidence angle can be assumed to be constant. In order to compare the I/F derived from the images with the theoretical model, it is necessary to compensate for this variation, which can be accomplished by using the normal I/F given by $(I/F)_{\perp} = (I/F).\mu$, where μ is the cosine of the emission angle (see Section 4).

Table 2
Saturn Physical Data[a]

Parameter	Value
m_S (g)	5.69×10^{29}
radius (km)	60330
J_2	1.6298×10^{-2}
J_4	-9.15×10^{-4}
J_6	1.03×10^{-4}

Note.
[a] Campbell & Anderson (1989).

3. Ring Lifetime

We performed a set of three-dimensional numerical simulations in order to study the orbital evolution of a sample of particles encompassing the orbits of Janus and Epimetheus. These particles are influenced by the gravity of Saturn, including the terms dues to J_2, J_4, and J_6, and the gravitational perturbations of Janus and Epimetheus. As we are dealing with μm-sized particles, the force due to the solar radiation pressure was also included in the numerical simulations (Sfair et al. 2009). This force can be given by the radiation pressure factor as

$$\beta = 5.1 \times 10^{-5} \frac{Q_{\rm pr}}{\rho r},$$

where ρ is the particle density, r its radius, and $Q_{\rm pr}$ is the radiation pressure coefficient assumed to be the unit (ideal material; Burns et al. 1979).

The numerical integrations were made with the Burlish-Stoer integrator and carried out using the Mercury package (Chambers 1999) with some modifications to include the solar radiation components (Sfair et al. 2009). Saturn's orbit is sufficiently close to circular that we will assume a constant solar flux. We did not consider the reflected sunlight from the planet and the Yarkvovsky effect on the dust particles, as their effects are small enough to neglect (Hamilton & Krivov 1996). Tables 2 and 3 show the adopted values for Saturn, Janus, and Epimetheus. We also considered the gravitational effects of the satellites Mimas, Tethys, Enceladus, Dione, and Titan. The initial conditions of these satellites were generated from the *JPL Horizons System* at the same epoch (JD 2453005.5) as was used for Janus and Epimetheus.

The test particles were equally distributed along 50 different values around the initial semimajor axis of Epimetheus (see Table 3), $a_E \pm 500$ km. The particles' initial mean anomalies were placed between 0° and 360° in steps of 1°. The initial eccentricity and inclination of these particles were adopted to have the same values as those of Epimetheus, as the values of these two orbital elements are larger than the eccentricity and inclination of Janus. The initial values of the argument of pericenter and longitude of the ascending node were also the same as those of Epimetheus. The choice of such a set of initial conditions was based on the idea of having particles that would have an orbital behavior similar to the co-orbital satellites. Each

Table 3
Janus and Epimetheus Data

	Janus	Epimetheus
m[a]	$5.83 \times 10^{-9}\, m_S$	$1.17 \times 10^{-9}\, m_S$
a[b](km)	151440	151490
e[b]	0.0068	0.0097
I[b] (deg)	0.16	0.35
ϖ[b] (deg)	287.60	41.11
Ω[b] (deg)	47.87	82.60
λ[b](deg)	90.59	278.15

Notes. m_S and m are the masses of Saturn and the satellites, respectively. a, e, I, ϖ, Ω, and λ are the semimajor axis, eccentricity, inclination, longitude of the pericenter, longitude of the ascending node, and the mean longitude, respectively.
[a] Thomas (2010)
[b] Jacobson et al. (2008).

particle was numerically integrated for 100 years. Each time the distance between the particle and one of the satellites is smaller than the radius of the satellite (88 km for Janus and 58 km for Epimetheus), a collision is detected. The particle is assumed to escape the system when it encounters the outer edge of the F ring (140,612 km) or the inner edge of the G ring (166,000 km). All parameters (time, position, and velocity) were recorded during the numerical integrations. The radius of the particles ranges between 1 and 13 μm, each 1 μm. One set formed by 100 μm-sized particles was also considered. Therefore, the ring is composed of 18000 particles of each size. Figure 3 shows the lifetime of these μm-sized particles. Almost all of them collide with Janus or Epimetheus in less than 100 years. Just a few hundred of them are removed through encounters with the F or the G ring.

The larger particles are initially removed more rapidly by collisions (see Figure 3), but note that this has only a modest effect on the average particle's lifetime (see Figure 4). The relative velocities of the particles at the time they collide with one of the satellites (Janus or Epimetheus) are too low (<0.09 km s^{-1}) to produce ejecta that can leave the satellite's gravity (Krivov et al. 2003).

These calculations show that within only a few decades, the particles collide with Janus or Epimetheus, which is consistent with the results of a previous two-dimensional study that did not take into account the effects of the solar radiation pressure (Williams & Murray 2011). Due to the third dimension, in our more realistic model, the results show a fraction of particles surviving at least twice as long as those of Williams & Murray (2011)'s model. Therefore, the average lifetime of the ring particles is very short. The improbability that this is a temporary ring implies that it must be continuously replenished.

4. Particle Production

Because the ring particles that collided with Janus or Epimetheus had collision velocities that are at most on the order of just 100 meters per second, it is too low to eject material from the gravitational domain of the satellites (Krivov et al. 2003). Therefore, another mechanism to supply material to the ring is needed. Replenishment by ejecta produced by collisions between very energetic interplanetary dust particles and the host body has been widely described in the literature

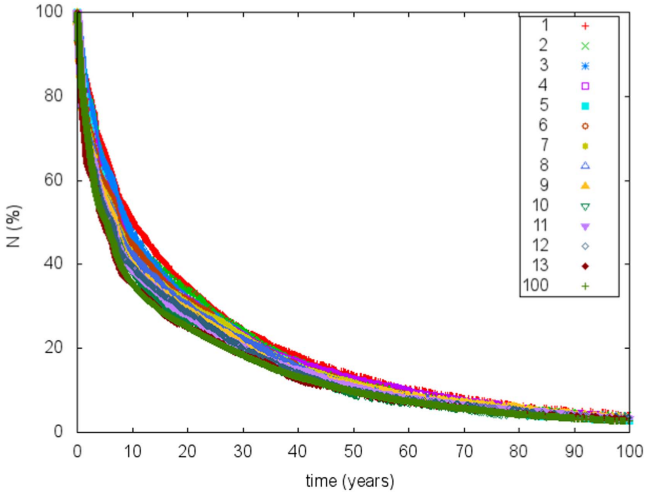

Figure 3. Temporal evolution of the remaining amount of particles (N) for different sizes. Each color or symbol indicates the size of the particle, from 1 to 13 μm, each 1 μm, and 100 μm.

for various targets, such as atmosphereless satellites (Krüger et al. 2000, 2003; Krivov et al. 2003) and the Pluto and Charon system (Stern 2009; Pires Dos Santos et al. 2013). We developed a physical model to verify whether material removed from the co-orbital satellites by interplanetary micrometeoroids impacts would be consistent with the observed ring.

Our physical model consists of a flux of interplanetary particles colliding with the satellites, generating ejecta (Krivov et al. 2003; Dikarev et al. 2006) that can supply material to replenish the Janus–Epimetheus ring. According to Poppe (2016), the averaged flux value that reaches the region of the satellites Janus and Epimetheus is $F_{\rm imp} = 3 \times 10^{-18}$ g cm^{-2} s^{-1}, where it was assumed that this flux is mainly composed of spherical particles of about 100 μm radius.

The amount of ejecta generated by the impacts on the surfaces of the satellites will depend on the dynamical conditions of the collisions and also on the physical characteristics of the impactor and the satellite. The rate of mass production can be given by (Dikarev et al. 2006)

$$\dot{M} = F_{\rm imp} Y S \eta,$$

where Y is known as yield, S is the cross section of the satellite, and η is given by $\eta = (V_0/V_{\rm esc})^{\gamma}$, with V_0 being the minimum ejecta velocity, $V_{\rm esc}$ being the escape velocity, and γ representing a slope, which assumes the value equals 2, considering the satellites with pure ice surfaces (Krivov et al. 2003). The value of the yield gives the ratio between the ejecta mass and the impactor mass. It is determined by experiments and can be given by

$$Y = 2.642 \times 10^{-5} m_{\rm imp}^{0.23} V_{\rm imp}^{2.46},$$

where $m_{\rm imp}$ and $V_{\rm imp}$ are, respectively, the mass and the velocity of the impactor. According to the above references, the value for the mass of the impactor is about 10^{-5} g. Note that in this model the ejected material will have a density similar to the target surface (pure ice). Table 4 presents the values of the rate of mass production, and other parameters, for each one of the satellites.

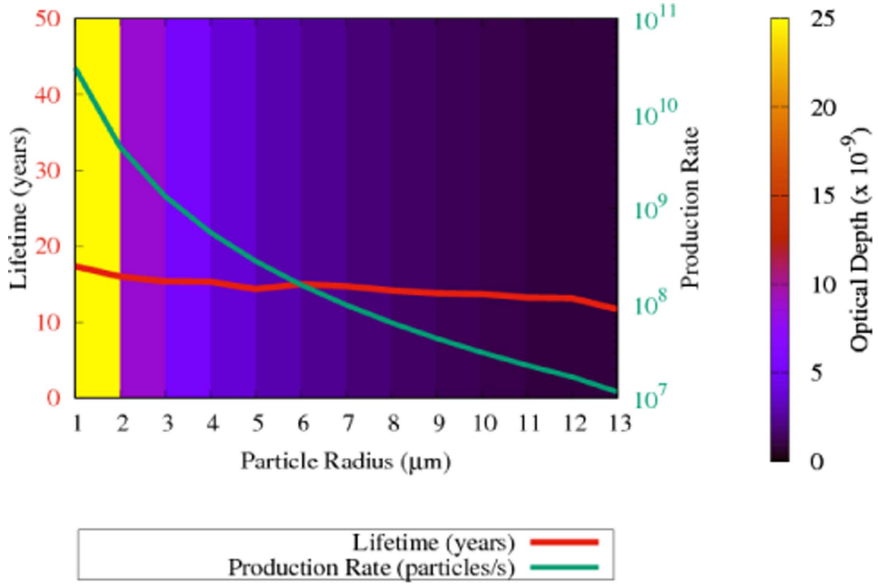

Figure 4. Normal optical depth values computed for each particle size range of the physical model (color-coded strips). The normal optical depth depends on the particle's production rate (green line), that decreases according to a power law and the particle's average lifetime (red line). The production rate is computed assuming a nominal impact flux of 3×10^{-18} g cm^{-2} s^{-1}. Note that the optical depth of this ring is dominated by the contribution of particles with radii between 1 and 4 μm. The average lifetime was obtained by the sum of the lifetime for each particle divided by the number of particles.

Table 4
Rate of Mass Production

Satellite	S(km^2)	V_0(m s^{-1})	V_{esc}(m s^{-1})	V_{imp}(km s^{-1})	η	$\dot{M}$(kg s^{-1})
Janus	2.52×10^4	28.5	53.0	23.41	0.287	5.85×10^{-3}
Epimetheus	1.01×10^4	28.5	35.0	23.41	0.654	5.35×10^{-3}

Note. Cross section (S), the minimum ejection velocity (V_0), the escape velocity (V_{esc}), the impact velocity (V_{imp}), the parameter η, and the mass production rate ($\dot{M}$).

Table 5
Mean Lifetime (T^i_{life}) and Steady-state Mass (M)

$r_{min}(\mu m)$	$r_{max}(\mu m)$	T^i_{life}(years)	M(kg)	$\bar{A}^i(\mu m^2)$	τ^i
1	2	16.67	3.42×10^5	5.63	2.48×10^{-8}
2	3	15.67	1.82×10^5	18.14	1.09×10^{-8}
3	4	15.33	1.40×10^5	39.98	6.58×10^{-9}
4	5	14.81	1.17×10^5	62.10	4.47×10^{-9}
5	6	14.66	1.05×10^5	93.51	3.33×10^{-9}
6	7	14.86	9.78×10^4	131.22	2.67×10^{-9}
7	8	14.43	8.87×10^4	175.20	2.12×10^{-9}
8	9	13.97	8.15×10^4	225.48	1.72×10^{-9}
9	10	13.74	7.63×10^4	282.03	1.45×10^{-9}
10	11	13.44	7.15×10^4	344.83	1.23×10^{-9}
11	12	13.18	6.76×10^4	413.95	1.06×10^{-9}
12	13	12.40	6.13×10^4	489.37	8.87×10^{-10}

Note. Average cross-section area ($\bar{A}_i$) and normal optical depth (τ^i) for each one of the size ranges between 1 and 13 μm. The steady-state mass is computed assuming a nominal impact flux of 3×10^{-18} g cm^{-2} s^{-1}.

The steady-state mass resulting from such a process is given by the product of the rate of the mass production by the average lifetime of the particles, $M = \dot{M} T_{life}$.

The production rate of particles with mass between m and m_{max} can be inferred from (Krivov et al. 2003; Dikarev et al. 2006)

$$\dot{N}(>m) = \frac{1-q}{q} \frac{\dot{M}}{m_{max}} \left(\frac{m_{max}}{m} \right)^q,$$

where q is the slope of a power-law distribution. As can be seen in laboratory experiments, in most of the cases the value of this slope is 0.8 (Krivov et al. 2003; Krüger et al. 2003; Dikarev et al. 2006). The quantity m_{max} is the maximum particle mass of the ensemble that has the same size of the initial impactor, i.e., 100 μm. The number of particles for a given size range can be determined by multiplying $\dot{N}$ by the corresponding average lifetime, T_{life}, given in Table 5. In order to obtain the total size distribution, N, it is necessary to sum the values found for each particle size range (every one micrometer).

As the particle size increases, the production rate decreases according to a power law, while the average lifetime varies

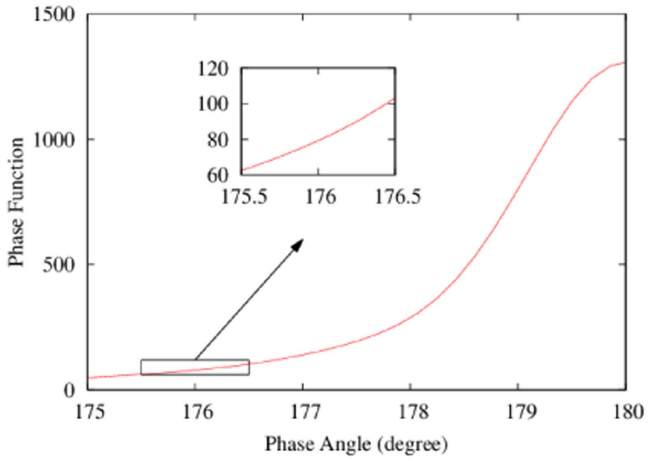

Figure 5. Phase function vs. phase angle. This is a phase curve for the particle size distribution given in Table 5. It was computed by using a numerical code developed for such a purpose (Wiscombe 1980). The inset shows a zoomed view illustrating how fast the phase function changes around 176°, which is near where the image data were obtained.

according to the particle size as shown in Figure 4. The combination of these two parameters leads to the ring's steady-state mass (Dikarev et al. 2006; Sfair & Giuliatti Winter 2012). We found that the normal optical depth, τ, of this steady-state ring primarily arises from the contribution of particles with radii between 1 and 4 μm (Figure 4).

4.1. Converting Produced Particles Into a Measurable Quantity (I/F)

In order to verify if the distribution of ring particles is compatible with the ring observed in *Cassini* images, we have to convert such distribution into a photometric quantity, I/F.

As seen before, the images that show the ring were taken at high phase angles ($\alpha > 175°$). Therefore, the ring is composed of small particles whose scattering properties can be well approximated with the Mie Theory. For high phase angles, the phenomenum that describes the observed light can be expressed through Chandrasekhar's equation (Chandrasekhar 1960). Considering that the ring is faint (normal optical depth, $\tau \ll 1$), I/F can be given by (Poulet et al. 2000)

$$I/F = \varpi_0 P(\alpha)\tau/4\mu,$$

where μ is the cosine of the emission angle, which was obtained from the images as being about 74°.8. $P(\alpha)$ and ϖ_0 are the phase function and the albedo of the particle population, respectively. The former shows how the particles scatter radiation in the direction of the observer, whereas the latter (also known as the reflection coefficient) is the ratio of reflected radiation from observed particles to incident radiation upon it. Both are computed by using a numerical code developed for such a purpose (Wiscombe 1980). This code depends on the wavelength of scattered radiation (634 nm), the refraction index, and the particle size distribution (found in the previous section). For an ice material without absorption, we have assumed that the real part of such an index is 1.309, and its imaginary part is zero.

Figure 5 shows how the phase function changes according to the value of α for the range between 175° and 180°. In order to obtain the value of I/F, we need to find the value of τ. The normal optical depth, τ, is given by the ratio between two areas:

$$\tau = A_{\rm cs}/A_{\rm ring},$$

where $A_{\rm cs}$ is the cross-section area resulting from all the visible particles that form the ring, and $A_{\rm ring}$ is the area in Saturn's equatorial plane that contains the ring. Assuming a triangular profile for the ring's brightness, we can approximate

$$A_{\rm ring} = (\pi/2)[(R_a + L/2)^2 - (R_a - L/2)^2] = 3.59 \times 10^9\ {\rm km}^2,$$

where R_a is the distance between the center of planet and the ring (152, 359.6 km), and L is the width of the ring (7500 km). The factor 2 in the above expression arises from the assumed shape of the profile.

The $A_{\rm cs}$ is computed through the addition of the cross-section areas of each particle of the ring. In order to do that, we divided the set of particles into 13 particle size ranges of 1 μm. Then, for each range, we obtained the average cross-section area, the average lifetime ($\bar{T}^i{}_{\rm life}$), and the difference of the rate production of range extremes ($\Delta\dot{N}^i_T$). By multiplying these three values and summing up the results for all ranges, we obtain

$$A_{\rm cs} = \sum_{i=1\leftrightarrow 2}^{12\leftrightarrow 13} \bar{A}^i \Delta\dot{N}^i_T \bar{T}^i_{\rm life} = 1.23 \times 10^4\ {\rm km}^2.$$

Thus, the total normal optical depth is given by

$$\tau = \sum_{i=1\leftrightarrow 2}^{12\leftrightarrow 13} \tau^i,$$

where τ^i is the normal optical depth due to each range of particles size. The values of $\bar{A}^i$ and τ^i are given in Table 5. Therefore, if $F_{\rm imp} = 3 \times 10^{-18}\ {\rm g\ cm^{-2}\ s^{-1}}$, then the total normal optical depth of the visible particle ring should be about 6×10^{-8}.

Therefore, for any given value of α, one can compute the I/F from the current model, where the albedo was always assumed to be equal to one. For example, for $\alpha = 175°.8$, the corresponding value of the phase function is about 70 (Figure 5). A comparison of the results of our model with the values obtained by photometry from a *Cassini* image is presented in Figure 6. It shows a curve (full black line) of the value of the normal I/F ($(I/F)_\perp = (I/F).\mu$) as a function of the phase angle (α) for our physical model. Note the large decrease in the value of $(I/F)_\perp$ as the phase angle reaches values only two or three degrees smaller than 180°. The blue dots in Figure 6 indicate photometric data obtained from the same *Cassini* image shown in Figure 1.

From the best ring image, considering its background level and the camera sensitivity, we can estimate that the ring is only visible by the *Cassini* spacecraft when it forms a phase angle (Sun-ring-*Cassini*) in the range from 140° to 180°. That has also been confirmed by the non-detection of the ring in observations of the same region made by *Cassini* at different geometries (red triangles). Thus, for the *Cassini* spacecraft orbiting around Saturn and pointing its camera toward the ring, the ring will "not be visible" most of the time (Figure 6). Therefore, we say that the ring behaves like a firefly. The analogy is that it can only be viewed by the spacecraft from time to time, when *Cassini*, the ring, and the Sun are arranged in a particular geometric configuration. Otherwise, it remains

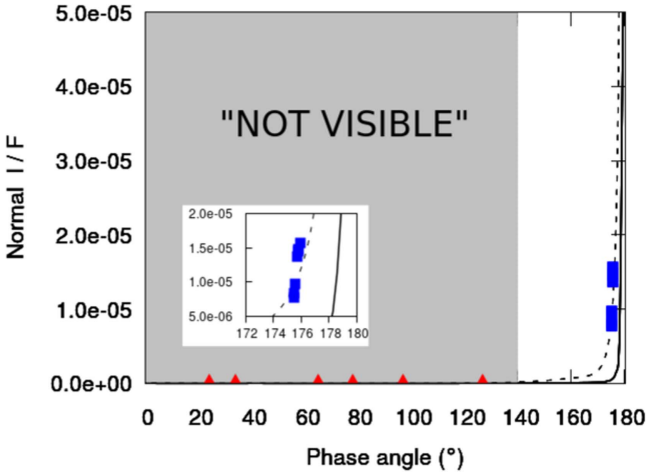

Figure 6. The visibility range: plot of $(I/F)_{\perp}$ as a function of the phase angle (α). The solid black line was derived from the physical model assuming a nominal impact flux of 3×10^{-18} g cm^{-2} s^{-1}, while the dashed line was derived assuming a flux one order of magnitude higher. Note the abrupt change in the values of $(I/F)_{\perp}$ as α gets close to 180°. The blue squares are data extracted from the same *Cassini* image shown in Figure 1 and their coordinates are given in Table 6. The red triangles indicate α of images where the ring could not be identified. For $0° \leqslant \alpha \leqslant 140°$ we have that $(I/F)_{\perp} \approx 0$ (gray zone). Therefore, despite of the J–E ring be a continuous full ring, it was only be seen by *Cassini*'s camera within a short arc of phase angle (>140°). The inset is a zoomed view showing how well the data fits the physical model.

Table 6
Pixels Coordinates from Image W1537029133

Coordinate X	Coordinate Y	Phase Angle (°)	$(I/F)_{\perp}$
103	264	175.49	7.8022e–06
103	259	175.50	8.3329e–06
104	251	175.52	9.6913e–06
126	219	175.70	1.3674e–05
139	209	175.80	1.4769e–05
141	208	175.81	1.4515e–05
156	198	175.92	1.5633e–05

Note. The origin of the coordinate system (0, 0) is at the lower left corner of the image.

"in the dark," not visible to *Cassini*'s cameras. Although a wider range of particles, in terms of size and quantity, might be found in the ring, only those particles in the range of 1–4 μm are responsible for almost all of the light captured by the *Cassini* spacecraft camera (Figure 4).

The physical model results (full black line in Figure 6) were generated with a micrometeoroids flux of 3×10^{-18} g cm^{-2} s^{-1}, which is the most up-to-date value found in the literature (Poppe 2016). From the zoomed panel in Figure 6 , we note that the values of the photometric data (blue dots) are not very well fitted by the physical model (full black line). However, this discrepancy is acceptable taking into account the uncertainties of the parameters involved. For instance, if we assume a flux one order of magnitude higher (dashed line), which is perfectly plausible, the physical model fits the observational data much more closely (zoomed panel in Figure 6). Consequently, this ring with very short lifetime particles can be accordingly replenished by particles generated through interplanetary micrometeoroid collisions with the surfaces of Janus and Epimetheus.

5. Conclusions

In this work, we performed a set of studies on the Janus–Epimetheus ring. From photometric analysis of *Cassini* images, we found that in most of the images, the ring extends along a wide longitude range, and a combination of just three of these images shows that the longitudes covered by the ring make an almost complete ring, not just a series of arcs. Furthermore, no significant variation in brightness with longitude was visually found. Thus, we conclude that this ring is continuous and smooth. The width of the ring is about 50% larger than previously announced (Porco et al. 2006).

In our search for *Cassini* images that could have observed the ring, we verified that it appeared only in high phase-angle images. What indicated the ring is mainly composed of micro-sized particles.

Then, we studied the lifetime of the ring particles. The results showed that within only a few decades, the particles collide with Janus or Epimetheus. Therefore, the lifetime of the ring particles is too short, suggesting the ring must be continuously replenished.

In order to provide such replenishment, we considered a collisional model of micrometeorites on the surface of the two satellites. As the particle size increases, the production rate decreases according to a power law, while the average lifetime is roughly constant around 15 years. The combination of these two parameters leads to the ring's steady-state mass. We found that the optical depth of this steady-state ring primarily arises from the contribution of particles with radii between 1 and 4 μm. The outcome of this model of particle production showed to be compatible with the Janus–Epimetheus ring data obtained from image analysis. The ring has also been identified at lower phase angles ($\sim$146° and $\sim$157°) with normal I/F at least one order of magnitude lower than those presented in this work (M. Hedman 2017, private communication). This is in full agreement with our results and conclusions.

The *Cassini* image data used in this work was provided by NASA's Astrophysics Data System. This work, which was supported by FAPESP (proc. 2011/08171-3, proc. 2016/24561-0), CNPq and CAPES, was improved by helpful discussions with Nilton do Rosario, Doug Hamilton, Roberto Vieira Martins, and Matthew Hedman. The authors would like to thank the generous referee that contributed significantly to the final version of this paper. The support from PROPE-UNESP is also acknowledged.

ORCID iDs

Othon C. Winter https://orcid.org/0000-0002-4901-3289

References

Burns, J. A., Lamy, P. L., & Soter, S. 1979, Icar, 40, 1
Campbell, J. K., & Anderson, J. D. 1989, AJ, 97, 1485
Chambers, J. E. 1999, MNRAS, 304, 793
Chandrasekhar, S. 1960, Radiative Transfer (New York: Dover)
Dermott, S. F., & Murray, C. D. 1981, Icar, 48, 12
Dikarev, V. V., Krivov, A. V., & Grün, E. 2006, P&SS, 54, 1014
Gumprecht, R. O., & Sliepcevich, C. M. 1953, JPhCh, 57.1, 90
Hamilton, D. P., & Krivov, A. V. 1996, Icar, 123, 503

Harrington, R., & Seidelmann, P. 1981, Icar, 47, 97
Jacobson, R. A., Spitale, J., Porco, C. C., et al. 2008, AJ, 135, 261
Krivov, A. V., Sremcević, M., Spahn, F., Dikarev, V. V., & Kholshevnikov, K. V. 2003, P&SS, 51, 251
Krüger, H., Krivov, A. V., & Grün, E. 2000, P&SS, 48, 1457
Krüger, H., Krivov, A. V., Sremcević, M., & Grün, E. 2003, Icar, 164, 170
Pires Dos Santos, P. M., Giuliatti Winter, S. M., Sfair, R., & Mourão, D. C. 2013, MNRAS, 430, 2761
Poppe, A. R. 2016, Icar, 264, 369
Porco, C. C., West, R. A., Squyres, S., et al. 2004, SSRv, 115, 363
Porco, C. C., & Cassini Imaging Science Team 2006, IAUC, 8759, 1
Poulet, F., Sicardy, B., Dumas, C., Jorda, L., & Tiphene, D. 2000, Icar, 145, 147
Sfair, R., & Giuliatti Winter, S. M. 2012, A&A, 543, A17
Sfair, R., Giuliatti Winter, S. M., Mourão, D. C., & Winter, O. C. 2009, MNRAS, 395, 2157
Stern, S. A. 2009, Icar, 199, 571
Synnott, S. P., Peters, C. F., Smith, B. A., & Morabito, L. A. 1981, Sci, 212, 191
Thomas, P. C. 2010, Icar, 208, 395
Treffenstädt, L. L., Mourão, D. C., & Winter, O. C. 2015, A&A, 583, A80
van de Hulst, H. C. 1957, Light Scattering by Small Particles (New York: Wiley)
Williams, G. A., & Murray, C. D. 2011, Icar, 212, 275
Wiscombe, W. J. 1980, ApOpt, 19, 1505
Yoder, C. F., Colombo, G., Synnott, S., & Yoder, K. 1983, Icar, 53, 431